Composites Part C: Open Access 5 (2021) 100152

Contents lists available at ScienceDirect

Composites Part C: Open Access

journal homepage: www.elsevier.com/locate/jcomc

Theoretical approximation of hydrodynamic and fiber-fiber interaction forces for macroscopic simulations of polymer flow process with fiber orientation tensors

Florian Wittemann [a,*], Luise Kärger [a], Frank Henning [a,b]

[a] Karlsruhe Institute of Technology (KIT), Institute of Vehicle System Technology, Lightweight Technology, Rintheimer Querallee 2, 76131, Karlsruhe, Germany
[b] Fraunhofer Institute for Chemical Technology (ICT), Joseph-von-Fraunhofer-Straße 7, 76327 Pfinztal, Germany

ARTICLE INFO

Keywords:
Discontinuous fiber reinforced polymers
Injection molding simulation
Fiber-fiber interactions
Hydrodynamic forces

ABSTRACT

Flow processes of discontinuous fiber reinforced polymers (FRPs) are the essence of several polymer-based manufacturing processes. FRPs show a transient chemo-thermomechanical matrix behavior and fiber-induced anisotropic physical properties. Therefore, they are one of the most complex materials used in volume production. The general flow behavior is influenced by fibers and their interactions with the matrix and other fibers. The consideration of individual fibers is numerically not capable for process simulation of FRP parts. Therefore, orientation tensors are used in macroscopic simulations, leading to a loss of information about the fiber network. Within this work, novel approximation schemes are presented to determine hydrodynamic and fiber-fiber contact forces with information provided by the second order fiber orientation tensor. Approximation of these forces can henceforth facilitate fiber breakage modeling in macroscopic process simulations. The results are verified by numerical simulations with individual fibers of different orientation states and lengths, showing good agreement with the verification results.

1. Introduction

Due to their possibility of low cost production and their lightweight potential, discontinuous fiber reinforced polymers (FRP) parts become more focused in automotive industry, even for structural parts [1]. Since the physical properties of the final part depend on manufacturing conditions, it is essential to perform an adequate process simulation, with special regards to fiber properties like orientation, length distribution and volume content. These aspects are relevant for an realistic structural simulation and optimization [2–4].

The presence of fibers should be regarded in simulations. Fiber orientation, length distribution and local volume content depend on flow field and therefore on the process parameters. In most cases the amount of fibers is too high to compute every single fiber. Therefore Advani and Tucker [5] developed a homogenization scheme to model orientation distributions with orientation tensors. This approach depends on a fourth order orientation tensor, which needs to be calculated with a closure approximation. For this purpose, the literature offers many different closure approximations of different complexity [6–8]. For modeling of flow-induced fiber orientation, most of the actual models are based on Jeffery's model for the movement of a single ellipsoid in a viscous fluid [9]. Folgar and Tucker expanded this approach to take fiber interactions into account, enabling the possibility to reach a steady state orientation [10]. The Folgar-Tucker model is the base for various models with different focuses. Nowadays the most common models are the RSC-model by Wang et al. [11] for highly filled materials and ARD-model by Phelps and Tucker [12] for long-fiber materials. Besides these semi-empirical approaches, the fiber movement (and hence orientation) can be modeled on micro or meso scale by calculating the hydrodynamic forces acting to the fibers from the matrix, as shown in [13,14]. Nevertheless, these approaches come along with high numerical effort, since the forces act on single fibers. To reduce the numerical effort, Meyer et al. [13] apply and verify the method by regarding only fiber bundles for a compression molding process. Although this method shows good results for SMC compression molding, it would not be meaningful for injection molding simulations, since the fibers in the material are suspended homogeneously in the matrix and not in bundles [15].

Other studies show that fiber-fiber interaction forces like lubrication, friction and normal forces have significant influence on fiber behavior during processing [16–19]. These forces act at every contact point of two fibers. The average number of contact points of one fiber can be determined according to Toll [20] depending on orientation and volume fraction. While the friction force is typically assumed to be of Coulomb type, several approaches with different complexity exist for calculation of lu-

* Corresponding author: FAST-LT, Building 70.04, Room 113, Rintheimer Querallee 2, 76131 Karlsruhe Germany.
E-mail address: florian.wittemann@kit.edu (F. Wittemann).

https://doi.org/10.1016/j.jcomc.2021.100152
Received 24 February 2021; Received in revised form 27 April 2021; Accepted 4 May 2021

brication force, taking single fibers, matrix viscosity or simple relative velocity into account [21–23]. By consideration of interaction forces, new models to describe the rheological behavior of FRPs and the influence of interaction on fiber orientation are developed [17,22].

The present work presents an extension of the anisotropic simulation method presented by Wittemann et al. [24] and builds on a reinforced injection molding simulation framework implemented in OpenFOAM [25]. The anisotropic fourth-order viscosity tensor in [24] considers the influence of fibers on the matrix/flow, representing the fiber-to-fluid part in the balanced stress distribution. However, its counterpart, the hydrodynamic forces acting from the fluid on the fibers, and the fiber-fiber interaction forces, are not mentioned. In the present work as well as in [24], the orientation tensor is used for fiber orientation modeling, to keep the numerical effort in an acceptable range. In addition to [24], novel approaches to approximate hydrodynamic and fiber-fiber interaction forces are developed and integrated in the simulations. These include hydrodynamic drag and lift forces as well as friction and lubrication forces. The latter act on fiber-fiber contact points, which are also approximated depending on fiber volume fraction, aspect ratio and orientation state. All needed information is deduced from the second order orientation tensor. Reference fibers are represented by the eigenvectors of the orientation tensor and the mentioned forces are acting on these reference fibers. The approaches for force calculation are verified in numerical studies based on randomly created individual fibers, representing different orientation states and fibers lengths.

2. Theory

The calculation of fluid-fiber and fiber-fiber interaction forces is based on macroscopic fiber orientation modeling, which is therefore shortly outlined at the beginning of this section. Afterwards, the hydrodynamic forces are calculated, acting from fluid on fibers and representing the counterpart of the anisotropic viscosity tensor [24] in the balanced stress distribution. Furthermore, approaches to quantify the fiber-fiber contact points are presented to calculate friction and lubrication forces between fibers. The calculation of the lubrication force builds on a novel approach depending on the average fiber-fiber overlap. This also includes an approach to determine the average fiber-fiber angle within a fiber network.

2.1. Fiber orientation modeling

As mentioned, the majority of actual orientation models for FRPs is based on Jeffery' Equation [9], describing the evolution of a single fiber by

$$\frac{d\boldsymbol{p}}{dt} = \boldsymbol{W}\boldsymbol{p} + \frac{r^2-1}{r^2+1}(\boldsymbol{D}\boldsymbol{p} - \boldsymbol{p}(\boldsymbol{p}\boldsymbol{D}\boldsymbol{p})), \tag{1}$$

with $\boldsymbol{p}$ being the normed orientation vector of the fiber, r is the fiber's aspect ratio and $\boldsymbol{D}$ and $\boldsymbol{W}$ are the strain-rate and vorticity tensor. Since the numerical effort to calculate the orientation of every single fiber is too high, Advani and Tucker [5] present a homogenization scheme, representing the fiber orientation by second and fourth order orientation tensors $\boldsymbol{A}$ and $\mathbb{A}$ given by

$$\boldsymbol{A} = \int \psi(\boldsymbol{p})\boldsymbol{p}\boldsymbol{p}d\boldsymbol{p} \tag{2}$$

and

$$\mathbb{A} = \int \psi(\boldsymbol{p})\boldsymbol{p}\boldsymbol{p}\boldsymbol{p}\boldsymbol{p}d\boldsymbol{p}, \tag{3}$$

with the probability density function $\psi(\boldsymbol{p})$ for a specific orientation. Several evolution models for $\boldsymbol{A}$ have been developed with different specification focusing on different materials and processes. Within this work the RSC-model developed by Wang et al. [11] is used, being well suited for highly fiber-filled materials and describing $\boldsymbol{A}$ by

$$\frac{d\boldsymbol{A}}{dt} + \frac{\partial \boldsymbol{u}\boldsymbol{A}}{\partial \boldsymbol{x}} = \boldsymbol{W}\boldsymbol{A} - \boldsymbol{A}\boldsymbol{W} + \frac{r^2-1}{r^2+1}\{\boldsymbol{D}\boldsymbol{A} - \boldsymbol{A}\boldsymbol{D} - 2[\mathbb{A} + (1-\kappa)(\mathbb{L} - \mathbb{M}\mathbb{A})]\boldsymbol{D}\} + 2\kappa C_{\mathrm{I}}\dot{\gamma}(\boldsymbol{\delta} - 3\boldsymbol{A}), \tag{4}$$

Here, $\boldsymbol{u}$ is the velocity, κ and C_{I} are the material specific strain-reduction factor and interaction coefficient, $\dot{\gamma}$ is the scalar shear-rate and $\boldsymbol{\delta}$ is the unity tensor. The tensors $\mathbb{L}$ and $\mathbb{M}$ are determined with the eigenvectors and eigenvalues of $\boldsymbol{A}$ as described in [11]. The IBOF5 closure approximation presented by Chung and Kwon [8] is chosen to determine $\mathbb{A}$.

Of course, information of individual fibers is lost within the usage of orientation tensors. But the eigenvectors $\boldsymbol{v}_n$ of $\boldsymbol{A}$ may be regarded as reference fibers, with the corresponding eigenvalues λ_n as orientation probability. The resulting formulation

$$\boldsymbol{A} = \sum_n \lambda_n \boldsymbol{v}_n \boldsymbol{v}_n \tag{5}$$

is identical to Eq. (2) in case of three fibers. Here the index n indicates the number of the eigenvector or corresponding eigenvalue. Since there are always three eigenvectors, it is $n \in \{1, 2, 3\}$. Additionally, restrictions are $\boldsymbol{A} \in \mathrm{sym}$, so $\boldsymbol{v}_n \perp \boldsymbol{v}_m$ and $|\boldsymbol{v}_n \cdot \boldsymbol{v}_m| = 0$ for $n \neq m$. Furthermore, it is $|\boldsymbol{v}_n \times \boldsymbol{v}_m| = 0$ for $n = m$ and the eigenvectors are normed, so all other cross and dot products are equal to 1.

2.2. Calculation of hydrodynamic forces from fluid on fibers

This section describes two approaches to compute the longe range hydrodynamic forces, acting from the fluid on the fibers, as for example also described in [13,26,27]. Contrary to these studies, the average force will be approximated on macroscopic scale within this work. Due to the orientation tensor, no position or orientation of individual fibers is known. Nevertheless, the average hydrodynamic force $\boldsymbol{F}^{\mathrm{h\_av}}$ can be determined with well known averaging methods. Dinh and Armstrong [27] for example give the hydrodynamic force on a fiber by

$$\boldsymbol{F}^{\mathrm{h}} = \Delta\boldsymbol{u}\left(\zeta_{\mathrm{t}}(\boldsymbol{\delta} - \boldsymbol{p}\boldsymbol{p}) + \zeta_{\mathrm{p}}\boldsymbol{p}\boldsymbol{p}\right), \tag{6}$$

with ζ_{t} and ζ_{p} being the transverse and parallel drag coefficient of the fiber and $\Delta\boldsymbol{u}$ is the relative velocity of fiber and fluid. To determine the average force, Eq. (6) must be integrated over all possible orientations, weighted with the corresponding orientation probability as described by Advani and Tucker [5]. By considering Eq. (2) and Eq. (5) it is

$$\begin{aligned}\boldsymbol{F}^{\mathrm{h\_av}} &= \oint \psi(\boldsymbol{p})\Delta\boldsymbol{u}\left(\zeta_{\mathrm{t}}(\boldsymbol{\delta} - \boldsymbol{p}\boldsymbol{p}) + \zeta_{\mathrm{p}}\boldsymbol{p}\boldsymbol{p}\right)d\boldsymbol{p} \\ &= \Delta\boldsymbol{u}\left(\zeta_{\mathrm{t}}\left(\boldsymbol{\delta} - \oint \psi(\boldsymbol{p})\boldsymbol{p}\boldsymbol{p}d\boldsymbol{p}\right) + \zeta_{\mathrm{p}}\oint \psi(\boldsymbol{p})\boldsymbol{p}\boldsymbol{p}d\boldsymbol{p}\right) \\ &= \Delta\boldsymbol{u}\left(\zeta_{\mathrm{t}}(\boldsymbol{\delta} - \boldsymbol{A}) + \zeta_{\mathrm{p}}\boldsymbol{A}\right) \\ &= \Delta\boldsymbol{u}\left(\zeta_{\mathrm{t}}\left(\boldsymbol{\delta} - \sum_n \lambda_n \boldsymbol{v}_n\boldsymbol{v}_n\right) + \zeta_{\mathrm{p}}\sum_n \lambda_n\boldsymbol{v}_n\boldsymbol{v}_n\right),\end{aligned} \tag{7}$$

since it is $\oint \psi(\boldsymbol{p})d\boldsymbol{p} = 1$. Hence, the average force on fibers within one element can be represented by the averaging of single fibers, considering the orientation tensor or use the eigenvalues and eigenvectors, since all three formulation are identical.

The approach Dinh and Armstrong [27] is not suited to distinguish between drag and lift force within a macroscopic simulation with homogenized material. Therefore, also the work of Meyer et al. [13] is considered, modeling hydrodynamic drag and lift force for fiber bundles within a compression molding process simulation. As shown in Eq. (7), the average forces can be represented by the eigenvectors and eigenvalues of the orientation tensor, which will be also applied on the approach of Meyer et al. The hydrodynamic forces are calculated for three reference fibers in each element. The reference fibers are represented by the

eigenvectors of the second order orientation tensor. The total hydrodynamic force acting on the n-th eigenvector $\boldsymbol{F}_n^{\mathrm{h}}$ is a combination of drag force $\boldsymbol{F}_n^{\mathrm{d}}$ and lift force $\boldsymbol{F}_n^{\mathrm{li}}$, since fibers are non-spherical. The drag force is derived from Stokes' law by

$$\boldsymbol{F}_n^{\mathrm{d}} = 6\pi\eta_{\mathrm{M}}\tilde{R}_n\Delta\boldsymbol{u} \tag{8}$$

where η_{M} is the matrix viscosity, $\tilde{R}_n$ is the radius of a sphere and $\Delta\boldsymbol{u}$ is the relative velocity between the sphere and the surrounding fluid. Within this work, the drag force acts on cylinders (fibers) with aspect ratio r and not on a sphere, so $\tilde{R}_n$ is approximated with

$$\tilde{R}_n = {}^{d}/_{2} \cdot k_n^{\mathrm{d}} = {}^{d}/_{2} \cdot \left[1 - \alpha(r-1)\cos\left(2\theta_n\right) + \beta(r-1)\right] \tag{9}$$

and

$$\theta_n = \arccos\left(\frac{\Delta\boldsymbol{u}\cdot\boldsymbol{v}_n}{\|\Delta\boldsymbol{u}\|}\right) \tag{10}$$

where d is the fiber diameter, α=0.09 and β=0.3125. The description of k_n^{d}, as given by Eq. (9) represents a numerical fit for hydrodynamic forces on single fibers with different orientations and aspect ratios, within a given flow field. A detailed description and verification of this approximation is presented by Meyer et al. [13].

The material is homogenized and simulations are performed on a discretized mesh, hence the real velocity of the fibers is unknown in a macroscopic process simulation. Since no fiber-matrix separation is assumed, the velocity of fibers and fluid within one cell is identical in the simulations. Nevertheless, there is a relative velocity, due to the existence of the velocity gradient. For determination of $\Delta\boldsymbol{u}$, it is therefore assumed that fibers within a cell have (on average) the velocity of the respective cell center and that the surrounding fluid has the velocity of the surrounding cells. This is a simplification that is necessary due to homogenization. Analogous to [13], the relative velocity $\Delta\boldsymbol{u}$ is calculated as

$$\Delta\boldsymbol{u} = \sum_{k\,\in\,N}\frac{w^{kj}}{W^{j}}\left(\Delta\boldsymbol{u}_k - \Delta\boldsymbol{u}_j\right) \tag{11}$$

with $w^{kj} = \exp(-9d^{kj2}/(2l^2))$ and $W^{j} = \sum_{k\,\in\,N} w^{kj}$, where d^{kj} is the distance between the cell centers of cells j and k, and l is the respective fiber length. N is the number of regarded neighbor cells, depending on l and d^{kj}. It is chosen in the way that average d^{kj} is equal or larger than 1.5 times l, but at least a minimum of one generation of cell neighbors is always considered. The difference between [13] and this work is, that in [13] the velocity of the surrounding elements is set in relation to a 1D-fiber velocity, separated from the velocity of the fluid, creating fiber-matrix separation, while here the velocity of the surrounding cells is set in relation to a cell with homogenized material, without fiber-matrix separation.

The lift force

$$\boldsymbol{F}_n^{\mathrm{li}} = 6\pi\eta_{\mathrm{M}}d/2k_n^{\mathrm{li}}\|\Delta\boldsymbol{u}\|[[\boldsymbol{q}]], \tag{12}$$

is also approximated with a coefficient

$$k_n^{\mathrm{li}} = \alpha(r-1)\sin\left(2\theta_n\right), \tag{13}$$

see Meyer et al. [13] for derivation and verification of k_n^{li}.

The direction $\boldsymbol{q}_n$ must be perpendicular to $\Delta\boldsymbol{u}$ and is defined as

$$\boldsymbol{q}_n = \left(\boldsymbol{v}_n \times [[\Delta\boldsymbol{u}]]\right) \times [[\Delta\boldsymbol{u}]], \tag{14}$$

where $[\![\cdot]\!]$ represents a normed vector defined as $[\![\cdot]\!] = \cdot/\|\cdot\|$. Finally, the total hydrodynamic force is defined as

$$\boldsymbol{F}_n^{\mathrm{h}} = \boldsymbol{F}_n^{\mathrm{d}} + \boldsymbol{F}_n^{\mathrm{li}} = 6\pi\eta_{\mathrm{M}}d/2\left(k_n^{\mathrm{d}}\Delta\boldsymbol{u} + k_n^{\mathrm{li}}\|\Delta\boldsymbol{u}\|[[\boldsymbol{q}_n]]\right). \tag{15}$$

In summary, $\boldsymbol{F}_n^{\mathrm{h}}$ is computed three times in each element, one for every eigenvector $\boldsymbol{v}_n$ and to be weighted with its corresponding eigenvalue λ_n.

2.3. Calculation of fiber-fiber interactions points

Toll [20] determines the contact points n_{c} of an average fiber in an arbitrary volume by

$$n_{\mathrm{c}} = {}^{8}/_{\pi}\phi r f + 4\phi(g+1), \tag{16}$$

with ϕ being the fiber volume fraction. Furthermore, the so-called specific number of contacts points $n_{\mathrm{c}\phi}$ is defined, so

$$n_{\mathrm{c}\phi} = {}^{8}/_{\pi}rf + 4(g+1) \tag{17}$$

and

$$n_{\mathrm{c}} = \phi n_{\mathrm{c}\phi}. \tag{18}$$

This definition will be needed in Section 2.4.

The scalar invariants of the orientation distribution f and g are given by

$$f = \oint\oint |\boldsymbol{p}_n \times \boldsymbol{p}_m|\psi(\boldsymbol{p}_n)\psi(\boldsymbol{p}_m)d\boldsymbol{p}_n d\boldsymbol{p}_m \tag{19}$$

and

$$g = \oint\oint |\boldsymbol{p}_n \cdot \boldsymbol{p}_m|\psi(\boldsymbol{p}_n)\psi(\boldsymbol{p}_m)d\boldsymbol{p}_n d\boldsymbol{p}_m. \tag{20}$$

Since this formulation depends on single fiber orientations, it is not capable for a macroscopic injection molding simulation. Férec et al. [17] present a possibility to compute f with the second and fourth order orientation tensor. Within their work g is neglected and therefore no approach is given.

Within this work two new approaches for determination of f and g are presented, based on the eigenvectors and eigenvalues of $\boldsymbol{A}$. Therefore, the number of fibers reduces to three for each regarded volume and f and g can be rewritten as

$$f = \sum_{n,m=1}^{3} |\boldsymbol{v}_n \times \boldsymbol{v}_m|\lambda_n\lambda_m \tag{21}$$

and

$$g = \sum_{n,m=1}^{3} |\boldsymbol{v}_n \cdot \boldsymbol{v}_m|\lambda_n\lambda_m. \tag{22}$$

Due to the restriction of $\boldsymbol{A} \in$ sym, mentioned in Section 2.1, the formulation of f and g can be simplified to

$$f = 3\pi/8\sum_{n\neq m}\lambda_n\lambda_m = 3\pi/8\left(2\lambda_1\lambda_2 + 2\lambda_1\lambda_3 + 2\lambda_2\lambda_3\right) \tag{23}$$

and

$$g = \lambda_n\lambda_n = \lambda_1\lambda_1 + \lambda_2\lambda_2 + \lambda_3\lambda_3. \tag{24}$$

The factor $3\pi/8$ is introduced in [17] to fit the analytical result of f for 3D-quasi-isotropic orientation. The eigenvector-based approach within this work (Eq. (21)) produces identical results for f compared to [17] (see Section 3.3 and the Appendix). Therefore, the factor is also used within this work to calculate the invariant f. The determination of the contact points can still be improved with the recognition of invariant g.

A critical look at Eq. (23) and Eq. (24) shows, that f and g can be represented by the eigenvalues and corresponding fitting parameters, like $3\pi/8$ in case of f. Of course, the results could be further improved by using more than one fitting parameter. Hence, the factors f and g can also be approximated with a polynomial fit, depending on the eigenvalues. Such a formulation is represented by

$$f = \sum_{n,m=1}^{3} M_{nm}\widetilde{\lambda_n}\widetilde{\lambda_m}, \tag{25}$$

with M_{nm}containing the polynomial coefficients and $\widetilde{\lambda_n} = (\lambda_1\ \lambda_2\ 1)$ to keep the function simple, since the information can be completely represented by two eigenvalues. The approximation for g is identical. The best fitting parameters for f and g are determined with a gradient-based optimization algorithm based on the results in Section 3.3.

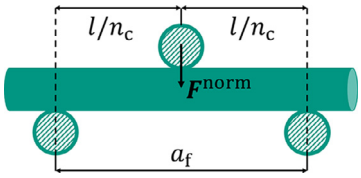

Fig. 1. One node for determination of $\boldsymbol{F}^{norm}$, including four fibers (green) with three contact points. The contact points are homogeneously distributed along the fiber.

2.4. Calculation of fiber-fiber interaction forces

The three forces appearing at every fiber-fiber contact point are friction force $\boldsymbol{F}^{fr}$, lubrication force $\boldsymbol{F}^{lu}$ and normal force $\boldsymbol{F}^{norm}$. The friction force is assumed to be of Coulomb type and defined as

$$\boldsymbol{F}^{fr} = k_{fr}\|\boldsymbol{F}^{norm\_av}\|\left[\left[\Delta\boldsymbol{u}_{fib}\right]\right] \tag{26}$$

with friction factor k_{fr} and the normalized relative velocity of two fibers $[[\Delta\boldsymbol{u}_{fib}]]$. The magnitude of the average normal force may be computed similar to [23,28,29] by

$$\|\boldsymbol{F}^{norm\_av}\| = \frac{32}{5\pi^2} E d^2 f^3 \phi^3, \tag{27}$$

with E being the elastic modulus of the fibers. Since the invariant g is approximated within the present work, the normal force can also be described with respect to g and not only to f. The average normal force given in Eq. (27) is presented by Toll and Månson [29]. They define the normal force by one so-called node, including three fiber-fiber contact points as illustrated in Fig. 1. Due to [29] the nodal force is given by

$$\|\boldsymbol{F}^{norm}\| = \int_0^{\phi} \frac{1}{\overline{a_f}\,\bar{s}} d\phi, \tag{28}$$

with $\overline{a_f}$ being the average node space (see Fig. 1) and $\bar{s}$ being the average nodal compliance, given by

$$\bar{s} = \frac{2\overline{a_f}^3}{\pi E d^4}\,. \tag{29}$$

According to Fig. 1 the average node space $\overline{a_f}$ is simply given by

$$\overline{a_f} = 2\frac{l}{n_c} = 2\frac{l}{\phi n_{c\phi}}. \tag{30}$$

Furthermore, the number of nodes per volume is given by

$$n_{node} = \frac{4\phi}{\pi d^2 \overline{a_f}}, \tag{31}$$

and the average normal force is given by

$$||\boldsymbol{F}^{norm\_av}|| = \frac{||\boldsymbol{F}^{norm}||}{n_{node} d}, \tag{32}$$

as shown by Toll and Månson [29]. To this point, no assumptions or simplifications about the number of contact points are made in [29], so Eqs. (28)-(32) can be used to calculate the normal force in the present work. Combining Eqs. (28)-(30) leads to

$$\boldsymbol{F}^{norm} = \int_0^{\phi} \frac{E d^4 \phi'^4 n_{c\phi}^4}{8 l^4} d\phi' = \frac{E d^4 \phi^5 n_{c\phi}^4}{40 l^4}. \tag{33}$$

So, the final average normal force is given by combining Eqs. (31)-(33) with

$$||\boldsymbol{F}^{norm\_av}|| = \frac{\pi E d^5 \phi^3 n_{c\phi}^3}{80 l^3} = \frac{\pi E d^5 \phi^3}{80 l^3}\left(8/\pi r f + 4(g+1)\right)^3. \tag{34}$$

It should be noted that in case of $n_{c\phi} = 8rf\,\phi/\pi$, which is the assumption within [29], Eq. (34) is identical to Eq. (27). By not neglecting the g-term, the average normal force and hence the friction force is predicted with more detail, especially in case of short fibers or high orientations, where g is more important.

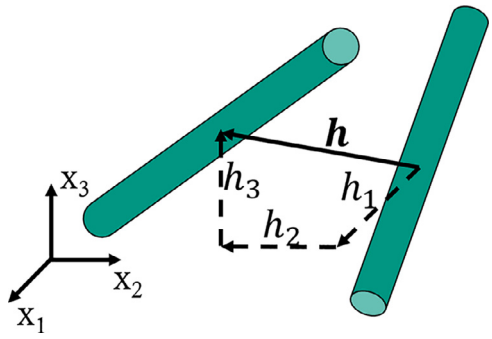

Fig. 2. Two fibers (green) with distance vector h, pointing from one fiber center two the other. Assumption of identical distance in all directions, so it is $h_1 = h_2 = h_3 = ||\boldsymbol{h}||/\sqrt{3}$.

Since the friction force is acting on microscopic scale, the relative velocity $\Delta\boldsymbol{u}$ (Eq. (11)) is not valid as relative velocity of two neighbor fibers. The relative velocity of two fibers centers in one cell is given by

$$\Delta\boldsymbol{u}_{fib} = \boldsymbol{D}\boldsymbol{h} = \begin{pmatrix} D_{11}h_1 + D_{12}h_2 + D_{13}h_3 \\ D_{21}h_1 + D_{21}h_1 + D_{23}h_3 \\ D_{31}h_1 + D_{31}h_1 + D_{33}h_3 \end{pmatrix}, \tag{35}$$

with $\boldsymbol{h}$ being the average distance vector between the fiber centers, as shown in Fig. 2.

By further assuming the fiber-fiber distance to be equal in every direction ($h_1 = h_2 = h_3 = ||\boldsymbol{h}||/\sqrt{3}$), which is an admissible simplification due to the homogenization, Eq. (35) can be simplified to

$$\Delta\boldsymbol{u}_{fib} = \frac{||\boldsymbol{h}||}{\sqrt{3}}\begin{pmatrix} D_{11}+D_{12}+D_{13} \\ D_{21}+D_{21}+D_{23} \\ D_{31}+D_{31}+D_{33} \end{pmatrix} = \frac{||\boldsymbol{h}||}{\sqrt{3}}\sum_{j=1}^{3} D_{ij} = \frac{||\boldsymbol{h}||}{\sqrt{3}}\Delta\tilde{\mathbf{u}}^{fib}, \tag{36}$$

The relative velocity is normalized for computation of the friction force, so $||\boldsymbol{h}||/\sqrt{3}$ can be neglected and the distance vector does not need to be determined. Finally, the friction force is given by Eq. (26) with the average normal force given in Eq. (34) and the relative velocity of two fibers given in Eq. (36).

Similar to [22,23] a linear model for lubrication force, depending on matrix viscosity η_M, projected overlapping area A_{ff} (Section 2.5, Eq. (40)) and relative velocity $\Delta\boldsymbol{u}_{fib}$ (Eq. (36)) is assumed. Furthermore and according to [22], the lubrication force is assumed to be reciprocal proportional to the fiber-fiber distance, since it vanishes for rising distances. Therefore, the lubrication force is defined as

$$\boldsymbol{F}^{lu} = \frac{k_{lu}}{||\boldsymbol{h}||/\sqrt{3}}\eta_M A_{ff}\frac{||\boldsymbol{h}||}{\sqrt{3}}\Delta\tilde{\mathbf{u}}_{fib} = k_{lu}\eta_M A_{ff}\Delta\tilde{\mathbf{u}}_{fib}, \tag{37}$$

with k_{lu} being the lubrication factor.

2.5. Calculation of projected fiber-fiber overlapping area

The projected overlapping area A_{ff} depends on the fiber-fiber angle φ and fiber diameter. Two cases must be separated, one is $\varphi \geq \varphi_{crit}$, where the area is a parallelogram (Fig. 3a and b), the other is $\varphi < \varphi_{crit}$, where the area is a hexagon, as shown in Fig. 3c. For most orientation states it is $\varphi > \varphi_{crit}$ making A_{ff} independent of fiber length, if the area is assumed to be not near the fiber ends.

For $\varphi \geq \varphi_{crit}$, A_{ff} is simply given by

$$A_{ff} = \frac{d^2}{\sin(\varphi)}. \tag{38}$$

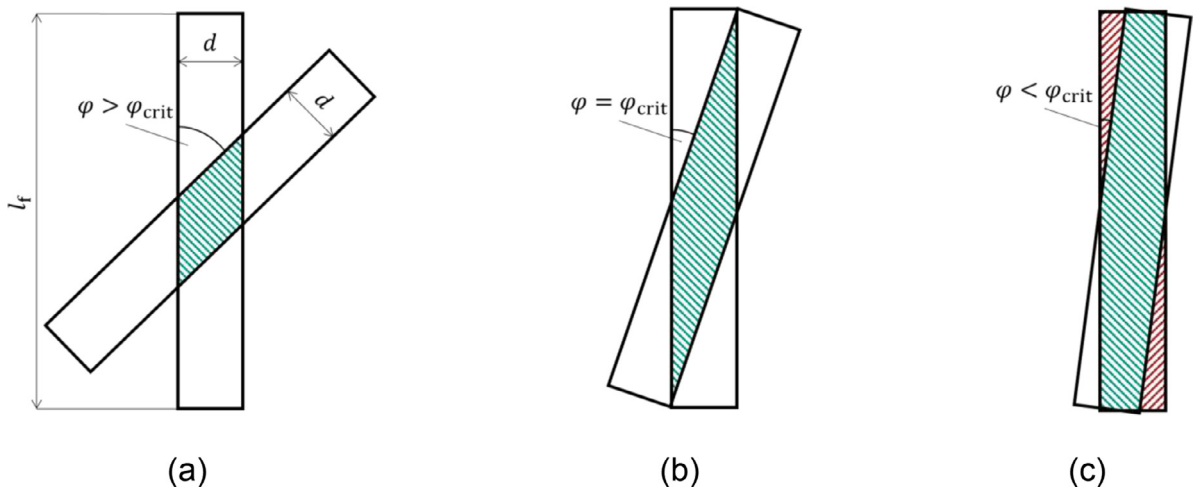

Fig. 3. Two overlapping fibers with highlighted overlap area (green). Abitrary angle $\varphi > \varphi_{crit}$ (a), critical angle φ_{crit} (b) and over-critical angle $\varphi < \varphi_{crit}$ (c). Red area is substracted for calculation of overlap.

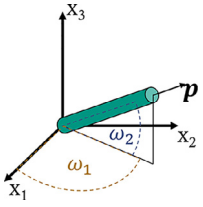

Fig. 4. Orientation of a single fiber (green), described by two angles ω_1 (ocher) and ω_2 (blue).

For $\varphi \leq \varphi_{crit}$ and realistic aspect ratios r, the assumption of small angles $\sin(\varphi) \approx \varphi$ can be made, resulting in $\varphi_{crit} = 2/r$. The overlap area (Fig. 3c green) can then be approximated by subtracting the red areas in Fig. 3c from the complete projected fiber surface area, so

$$A_{ff} = d^2 r - \frac{d^2 r^2}{4}\varphi. \tag{39}$$

Finally, the overlapping area is defined as

$$A_{ff} = \begin{cases} \frac{d^2}{\sin(\varphi)} & \text{for} \quad \varphi > \varphi_{crit} \\ d^2 r - \frac{d^2 r^2}{4}\varphi & \text{for} \quad \varphi \leq \varphi_{crit} \end{cases}. \tag{40}$$

The average angle φ within a fiber network can be approximated with f by

$$\varphi = {}^4/_{\pi} f, \tag{41}$$

where the factor ${}^4/_{\pi}$ is again introduced to fit the average angle of a 3D-quasi-isotropic orientation.

3. Results and Discussion

3.1. Individual fibers model for numerical verification

As verification cases, 22 different orientation states are regarded, each one built up from 500 randomly created individual fibers. The orientation of a single fiber is fully described by two angles ω_1 and ω_2, as shown in Fig. 4. To create different orientation states, the range of values for ω_1 and ω_2 is defined smaller for higher orientation state numbers. Orientation State 1 is '3D- quasi-isotropic', so $\omega_1 \in [0, \pi]$ and $\cos(\omega_2) \in [0, 1]$. In this way, the angle change is not identical in x_2- and x_3-direction, since injection molding parts are designed thin walled in most cases, so in one 'non-flow-direction' the degree of orientation orientation is lower than in the other.

The fibers are created using the 'rand' function within Matlab R2019a (creating a random value between zero and one), multiplied with the maximum values of ω_1 and $\cos(\omega_2)$ in the corresponding orientation state.

For the ongoing orientation states, the ranges are reduced by $\pi/20$ for ω_1 and $1/20$ for $\cos(\omega_2)$, until Orientation State 21, where $\omega_1 = \omega_2 = 0$, which represents the full alignment in x_1-direction. Orientation State 22 is a planar isotropic distribution in the x_1-x_2-plane ($\omega_1 \in [0, \pi]$ and $\omega_2 = 0$). Some examples of the orientation states with single fiber orientations and corresponding orientation tensors are shown in Fig. 5.

3.2. Numerical verification of hydrodynamic forces

To verify the approach presented in Section 2.2 for calculating the hydrodynamic forces based on eigenvectors, the acting forces are calculated twice: firstly, for 500 individual fibers and, secondly, for the corresponding orientation tensor. In this way, each orientation state is evaluated for two different relative velocities. Afterwards the average force is determined for the fibers ($\boldsymbol{F}^{\text{h\_av\_f}}$) and the eigenvector-based method ($\boldsymbol{F}^{\text{h\_av\_EV}}$). For the individual fibers, the average force is determined by

$$\boldsymbol{F}^{\text{h\_av\_f}} = 1/N \sum_{n=1}^{N} \boldsymbol{F}_n^{\text{h\_av\_f}}, \tag{42}$$

where N is total number of fibers, being 500 in this case and the orientation probability is $\psi(\boldsymbol{p}) = 1/N$. The average force of the eigenvectors is weighted with the corresponding eigenvalues so

$$\boldsymbol{F}^{\text{h\_av\_EV}} = \sum_{n=1}^{3} \lambda_n \boldsymbol{F}_n^{\text{h\_av\_EV}} \tag{43}$$

The relative velocities, matrix viscosity and fiber aspect ratio are chosen to be $\Delta\boldsymbol{u}_a = (1\ 0\ 0)$ m/s, $\Delta\boldsymbol{u}_b = (1/\sqrt{3}\ 1/\sqrt{3}\ 1/\sqrt{3})$ m/s, $\eta_M = 20$ Pa · s and $r = 100$. The results are shown in Fig. 6.

In Fig. 6a, the average drag force in dominant in x_1-direction, since this is the direction of $\Delta\boldsymbol{u}$. With higher degree of orientation, the drag force (acting in x_1-direction) decreases. $F_2^{\text{drag\_av}}$ and $F_3^{\text{drag\_av}}$ are zero since $\Delta u_2 = \Delta u_3 = 0$. In case of (planar) quasi-isotropic orientation or full alignment it is $F^{\text{lift\_av}} = 0$, due to the symmetric distribution of the orientation states to $\Delta\boldsymbol{u}$. $F_1^{\text{lift\_av}}$ and $F_3^{\text{lift\_av}}$ are about zero in general, since the orientation distribution in x_3-direction is always symmetric to $\Delta\boldsymbol{u}$ and the lift force is perpendicular to $\Delta\boldsymbol{u}$. The fibers are created randomly, hence the orientation is not exactly symmetric, and $F_3^{\text{lift\_av}}$ is no exactly zero.

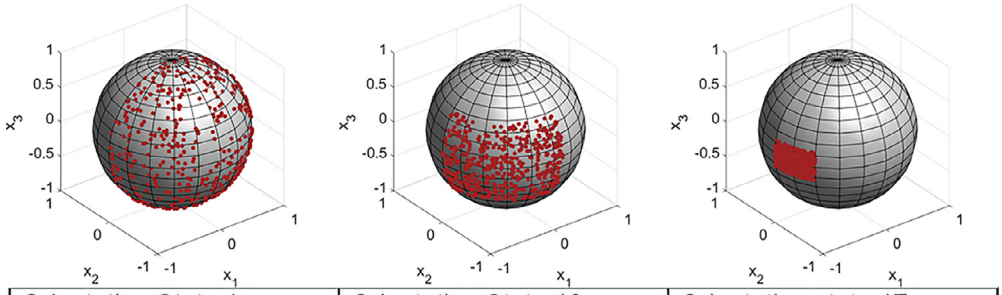

Orientation State 1 ‘3D-quasi-isotropic’	Orientation State 10 ‘mean orientated’	Orientation state 17 ‘high orientated’
$A_{ij} = \begin{bmatrix} 1/3 & 0 & 0 \\ & 1/3 & 0 \\ \text{sym.} & & 1/3 \end{bmatrix}$	$A_{ij} = \begin{bmatrix} 0.42 & 0.25 & 0.008 \\ & 0.47 & -0.015 \\ \text{sym.} & & 0.1 \end{bmatrix}$	$A_{ij} = \begin{bmatrix} 0.87 & 0.2725 & -0.0026 \\ & 0.12 & -0.0011 \\ \text{sym.} & & 0.01 \end{bmatrix}$

Fig. 5. Visualization of different orientation states with corresponding orientation state number and second order orientation tensor. Red dots are the orientations of the individual fibers on a unity sphere.

In Fig. 6b it is $F_1^{\text{drag\_av}} = F_2^{\text{drag\_av}} = F_3^{\text{drag\_av}}$ due to $\Delta u_1 = \Delta u_2 = \Delta u_3$. For quasi-isotropic orientation the lift force is again zero, based on the isotropic fiber distribution of the fibers towards the relative velocity. This is also the reason for $F_1^{\text{lift\_av}} = F_2^{\text{lift\_av}} = 0$ in case of planar isotropic orientation. Of course there are lift forces on individual fibers, but they cancel each other out during averaging, which is a disadvantage of the macroscopic approach.

As expected within Section 2.2 the average forces for the orientation averaging of individual fibers and for the eigenvector-based approach match exactly for both relative velocities. The force distribution with respect to orientation and relative velocity represents meaningful results, verifying the eigenvector-based method to be suitable to determine the average hydrodynamic force for an arbitrary orientation state. Nevertheless, the information cannot be set in relation to individual fibers again, but only to the reference fibers given by the eigenvectors.

3.3. Numerical verification of fiber-fiber contact points

The determination of contact points by eigenvectors and eigenvalues is verified by comparison to the calculations with individual fibers as described in Section 3.1 and to the approach of Férec et al. [17] (interaction tensor) for different orientation states and aspect ratios.

Within their work, Férec et al. present a second and fourth order interaction tensor to evaluate the total strain in a FRP. The second order interaction tensor is defined by

$$\boldsymbol{b} = \oint \oint \boldsymbol{p}_n \boldsymbol{p}_n |\boldsymbol{p}_n \times \boldsymbol{p}_m| \psi(\boldsymbol{p}_n) \psi(\boldsymbol{p}_m) d\boldsymbol{p}_n d\boldsymbol{p}_m. \tag{44}$$

Due to this definition, f is exactly given by

$$f = \text{trace}(\boldsymbol{b}) = \oint \oint |\boldsymbol{p}_n \times \boldsymbol{p}_m| \psi(\boldsymbol{p}_n) \psi(\boldsymbol{p}_m) d\boldsymbol{p}_n d\boldsymbol{p}_m. \tag{45}$$

Consequently, this formulation is also depending on single fiber orientations. Within [17] also an approximation to represent $\boldsymbol{b}$ with orientation tensors is given, so

$$\boldsymbol{b} = \boldsymbol{A} - \mathbb{A}\boldsymbol{A}. \tag{46}$$

Finally, the mentioned factor $(3\pi)/8$ is used to fit to the quasi-isotropic average value and $\boldsymbol{b}$ is defined by

$$b = \frac{3\pi}{8}(\boldsymbol{A} - \mathbb{A}\boldsymbol{A}). \tag{47}$$

So in case of the interaction tensor, the scalar invariant f is defined by

$$f_{\text{interactiontesnor}} = \text{trace}(\boldsymbol{b}) = \boldsymbol{\delta}\left(\frac{3\pi}{8}(\boldsymbol{A} - \mathbb{A}\boldsymbol{A})\right). \tag{48}$$

In a first step the computation of the scalar invariants f and g with eigenvectors and eigenvalues Eq. (23)-((25)) is verified. Therefore f and g are also determined with the individual fibers, using Eq. (19) and Eq. (20) as well as with the method presented in [17]. The second and fourth order orientation tensors are directly computed with the 500 individual fibers. The results are shown in Fig. 7. Due to the correction factor $3\pi/8$, introduced in Eq. (23) in Section 2.3, the results for the interaction tensor [17] and for the proposed eigenvector-based approach agree with the value of f for 3D- quasi-isotropic orientation. Both approaches show a rise of deviation for higher orientations, with a maximum of about 90 % for Orientation State 20 (highly aligned fibers in x_1-direction). For full alignment (Orientation State 21) both results are 0, and for planar isotropic distribution (Orientation State 22) the deviation is about 7.5 %. Both approaches give identical results, but for the general case the identity of the eigenvector method and the interaction tensor method can only be shown, if the relation between the fourth and the second order orientation tensor is exactly known, since it is necessary for computing the interaction tensor. The exact formulation of the fourth order orientation tensor is only defined for a few orientation states like 3D-quasi-isotropic and full alignment. The identity for these two cases is shown in the Appendix.

Table 1
Coefficients of polynomial fit of scalar invariants f and g.

Entry of M_{nm}	Value for approximating f	Value for approximating g
M_{11}	3.27	3.3011
M_{22}	-6.6744	0.4173
M_{33}	1.3475	1.5728
$M_{12} + M_{21}$	4.63897	4.2687
$M_{13} + M_{31}$	-4.5262	-3.8701
$M_{23} + M_{32}$	2.482	-1.9965

For the polynomial fit (Eq. (25)), the parameters are determined by a gradient-based optimization, based on the calculations with individual fibers. The resulting parameters are given in Table 1.The polynomial approximation of f is not zero for full alignment, nevertheless this case will not be reached in a real process. Besides full orientation, the maximum deviation is about 8.1 % for Orientation State 10. The mean square error is 0.0099 for the eigenvector-based and interaction tensor-based results and 0.00099 for the polynomial approximation, being 10 times smaller.

Fig. 7b shows the results of g for individual fibers, the eigenvector and the polynomial approach. The interaction tensor is not compared, since Férec et al. [17] does not propose an approach for g. The deviation of the eigenvector method to the solution with individual fibers is reciprocal to f, fitting for full alignment and having the maximum deviation for 3D- quasi-isotropic state. The maximum deviation is about 33 % and lower than the deviation for the calculation of f. For planar isotropic orientation, the deviation is about 20 %, being nearly three times higher compared to f. Due to the good agreement, no correction factor is used for determination of g. The polynomial approach shows the maximum

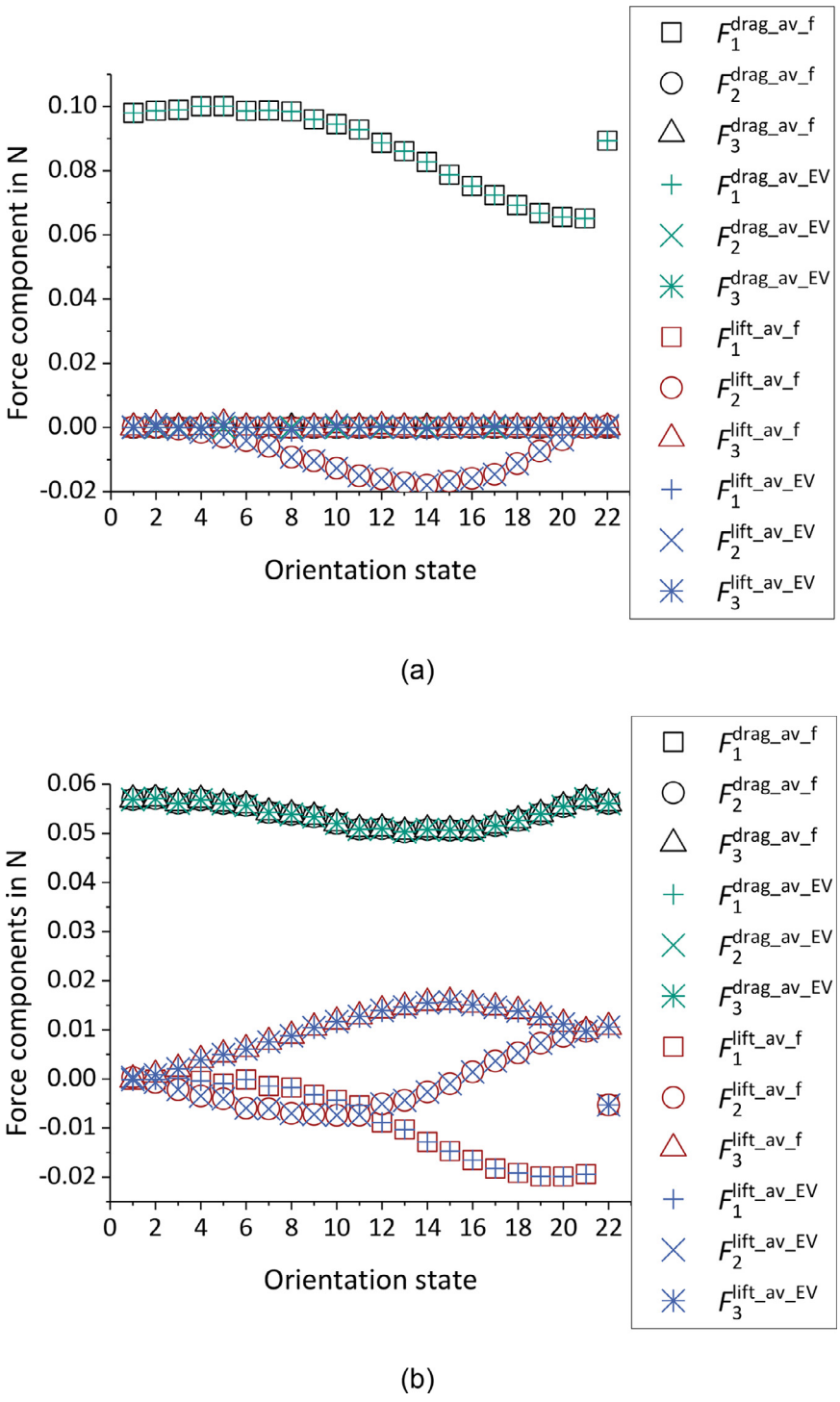

Fig. 6. Comparison of average hydrodynamic forces calculated with individual fibers (drag=black, lift=red) and orientation tensor (drag=green, lift=blue) for 22 different orientation states (cf. Figure 5). The relative velocities are $\Delta \boldsymbol{u}_a = (1\ 0\ 0)$ m/s (a) and $\Delta \boldsymbol{u}_b = (1/\sqrt{3}\ 1/\sqrt{3}\ 1/\sqrt{3})$ m/s (b).

deviation for planar isotropic orientation with about 2.5 %. The mean square error is 0.016 for the eigenvector based and 0.000033 for the polynomial approximation, being about 484 times smaller.

Fig. 8 compares the results for calculation of average fiber-fiber contact points according to Eq. (16). The results represent a fiber volume fraction of $\phi = 0.35$ and a fiber aspect ratio of $r = 10$ (Fig. 8a) or $r = 100$ (Fig. 8b). For both aspect ratios, the novel approaches are always closer to the individual fibers than the interaction tensor method [17], due to considering g, being more significant for small aspect ratios. The offset is $4\phi(g + 1)$, see Eq. (16). The recognition of g is more important for higher orientations, since g rises with the degree of orientation while f decreases.

Hence, the interaction tensor deviates more for higher orientation states, compared to the eigenvector-based approach, which is getting closer to the individual fiber solution again.

The polynomial approximation shows the best results for most orientation states, with slightly too high predictions for Orientation States 7-11 and for the planar isotropic Orientation State 22. The maximum deviation is observed at full alignment (State 21) with 29.2 % for r=10 and 291 % for r=100. Full alignment is the only orientation state, at

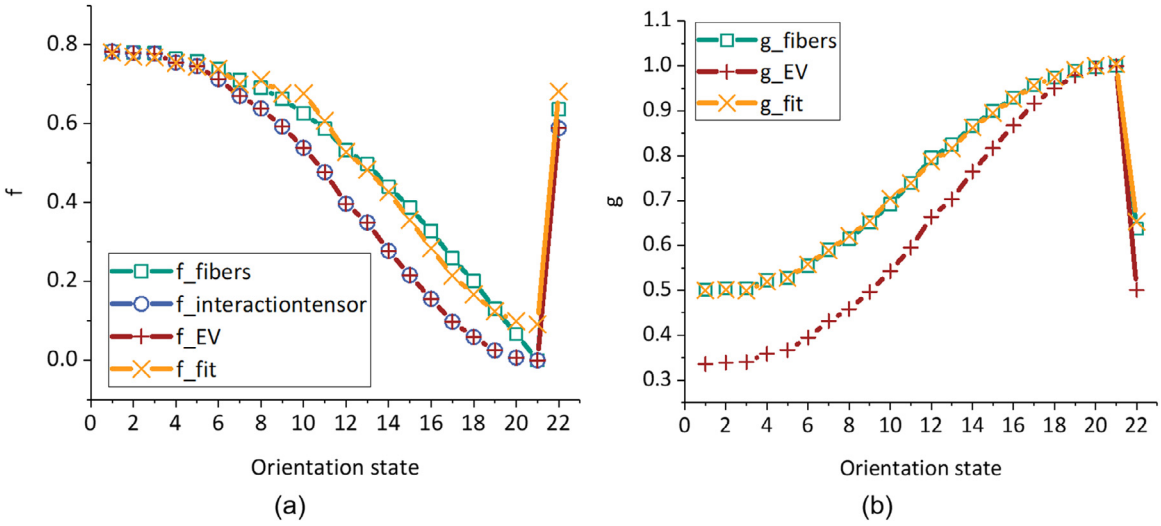

Fig. 7. Values of f (a) and g (b) for the different approaches. Comparisson of eigenvector approach (red,+) and polynomial approximation (yellow, ×) to solution with individual fibers (green,□) and interactions tensor based method presented in [17] (blue,○).

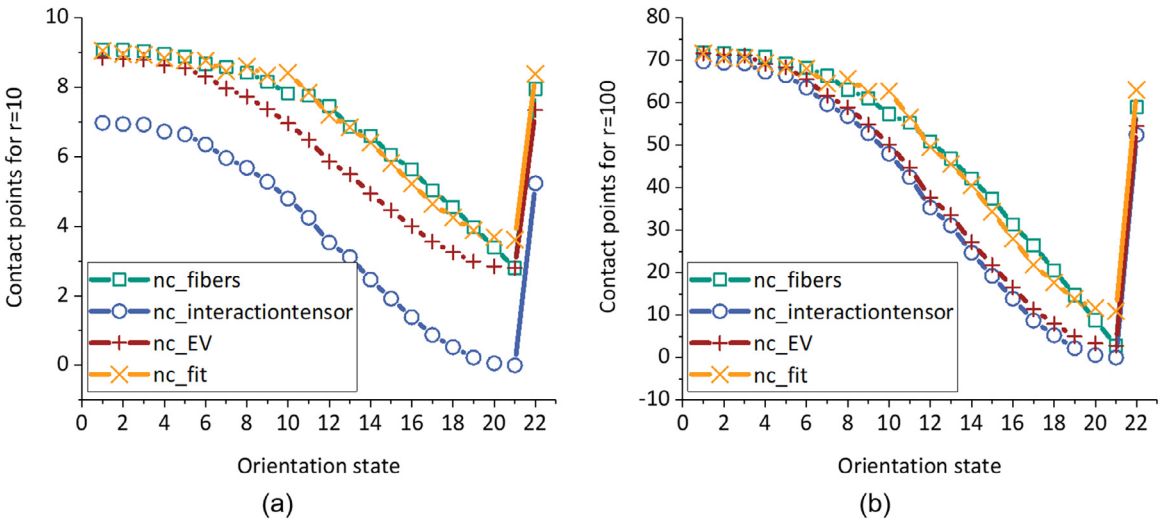

Fig. 8. Computed number of fiber-fiber contact points for ϕ=0.35 and r=10 (a) and r=100 (b). Comparisson of eigenvector approach (red,+) and polynomial approximation (yellow, ×) to solution with individual fibers (green,□) and interactions tensor based method presented in [17] (blue,○).

which the eigenvector method provides better results than the polynomial approximation. The maximum deviation of the eigenvector method is 29.4 % for r=10 at Orientation State 17 and 66 % for r=100 at Orientation State 19. The mean square error is about 1.0132 for r=10 and 82.85 for r=100 in the eigenvector case, while it is 0.0917 for r=10 and 8.85 for r=100 in the polynomial fit case, approximately 10 times lower for both aspect ratios.

In summary the results of the eigenvector approach are in acceptable agreement to the ones of the individual fibers and fit better than the current state of research. Therefore, Eq. (16), (23) and (24) are qualified for determination of fiber-fiber contact points. Nevertheless, the polynomial approximation provides significantly better results than the eigenvector-based approach. The better results of the polynomial approach are meaningful, since the input for both approaches is the same (eigenvalues), but the polynomial approach includes more individual fitting parameters. For the 3D-simulations in Section 4, consequently, the polynomial approach is used to determine the scalar invariants f and g.

3.4. Verification of fiber-fiber angle approximation

Similar to the contact points the approach to determine the average fiber-fiber angle is novel and must be verified. The mean angle is verified with the same 22 orientation states, computed with 500 individual fibers as described in Section 3.1.

There are 500 fibers per orientation state, one angle includes two fibers and the angle of a fiber with itself is not considered, hence, there are 124500 individual angles per orientation state. Afterwards, the average of these 124500 angles is built for comparison to Eq. (41).

The angle of two individual fibers $\boldsymbol{p}_n$ and $\boldsymbol{p}_m$ is given by

$$\varphi_{\text{fibers}} = \cos^{-1}\left(\boldsymbol{p}_n \cdot \boldsymbol{p}_m\right). \tag{49}$$

The f needed do determine the average angle with Eq. (41) is also computed with the individual fibers (Eq. (19)), since the aim of this section is to verify the approximation of the average angle not any approximation of f. The results are shown in Fig. 9. The predicted average angle fits well for orientation states with low numbers and is slightly

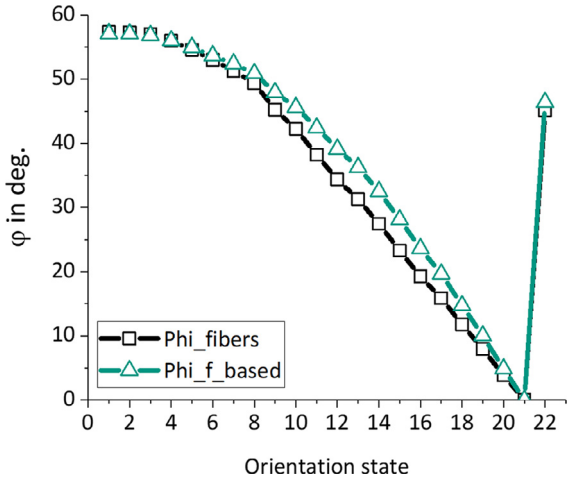

Fig. 9. Computed average fiber-fiber angle by averaging single angles of individual fibers (black, □) and approximation based on f given by Eq. (41) (green, Δ).

too high for higher orientation, having a maximum deviation of about 26 % for orientation state 20. The mean square error is 8.4587, so on average the approximation deviates about 2.26°. Eq. (41) is linear in f so the deviation when using an approximation for f corresponds to the deviation of the approximation towards the f computed with individual fibers.

3.5. Numerical verification of fiber-fiber overlap area

In a next step, the approximation of the fiber-fiber overlap area needs to be verified, being relevant for the calculation of the lubrication force. Again, the approximated results are compared to calculation with individual fibers explained in Section 3.1. For the individual fibers, the individual overlap areas are computed, based on Eq. (40). Here, the individual angles presented in Section 3.4 (Eq. (49)) are used, so there are 124500 overlap areas for each orientation state, which get averaged for comparison. Since the eigenvectors are always perpendicular to each other (see Section 2.1) the calculation of individual overlap areas is not meaningful for the eigenvector-based and the polynomial approximation approach. Therefore, Eq. (41) is used to determine the average φ and afterwards the average A_{ff} based on Eq. (40) for the orientation states and the two novel approaches is computed.

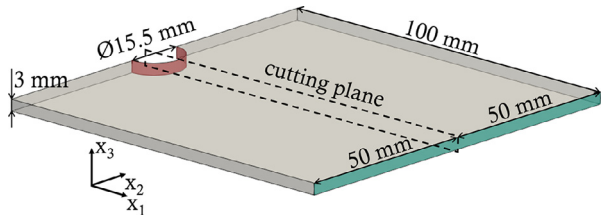

Fig. 11. 3D-Model for injection molding simulations. Square plate with circular inlet in red, outlet in green and cutting plane for results.

The results are shown in Fig. 10 for two different aspect ratios $r = 10$ (Fig. 10a) and $r = 100$ (Fig. 10b). Both approaches predict a too small overlap for low- number orientation states (<15) for both aspect ratios. While the calculated area is too high for the eigenvector-based approach for higher orientation states (>15), the polynomial fit predicts well. One exception is again full alignment, where the eigenvector-based approach fits perfect and the polynomial approach shows is maximum deviation with about 28 % for $r = 10$ and about 870 % for $r = 100$, again, this orientation state will not be reached in a real process. The deviation of planar-isotropic orientation in case of polynomial fit is about 75 % for $r = 10$ and about 184 % for $r = 100$, while it is about 65 % for $r = 10$ and about 164 % for $r = 100$ in case of the eigenvector-based method. Besides full alignment and planar-isotropic, the maximum deviation of the polynomial approach is about 41 % for $r = 10$ and about 55 % for $r = 100$ at orientation states 10 and 11, while it is about 44 % for $r = 10$ and about 73 % for $r = 100$ at orientation states 17 and 20 for the eigenvector approach. The mean square error of the polynomial fit is 2.5e-14 for $r = 10$ (1.45e-14 without full alignment) and 1.84e-11 for for $r = 100$ (3.3e-13 without full alignment).

For the eigenvector-based approach it is 6e-14 for $r = 10$ (6.4e-14 without full alignment) and 8.5e-12 for $r = 100$ (8.8e-12 without full alignment). Ignoring the unrealistic case of full alignment, the polynomial approach creates the better results with a mean square error being about 4.4 times smaller for $r = 10$ and about 26.6 times smaller for $r = 100$, compared to the eigenvector-based approach. In general, both approaches are able predict the overlap area quite adequate, where

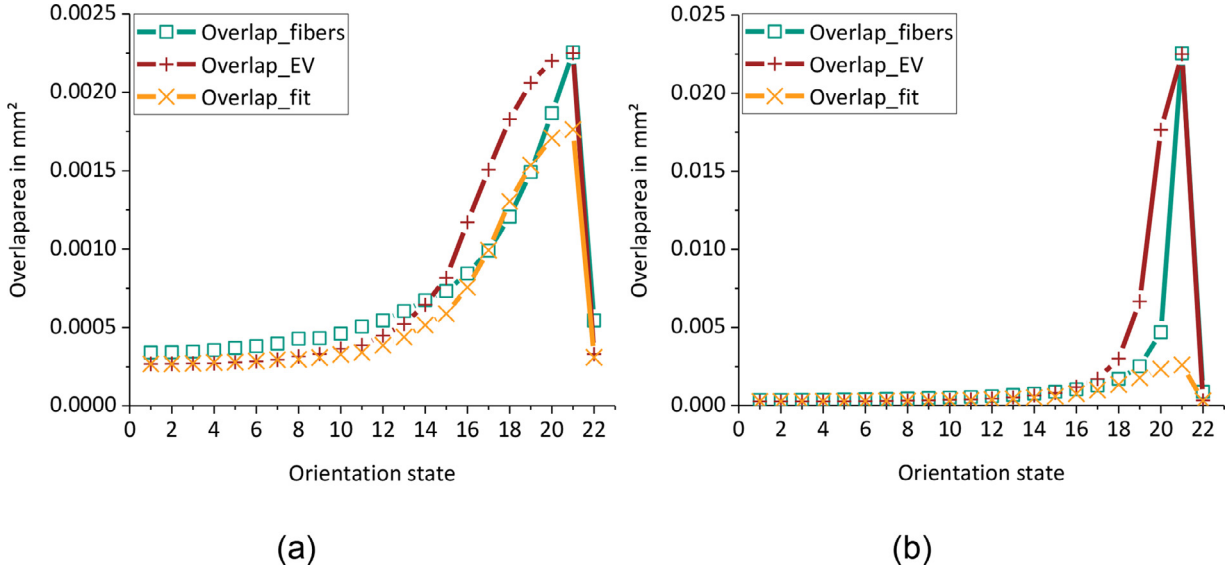

Fig. 10. Computed average fiber-fiber overlap area in mm² for r=10 (a) and r=100 (b). Comparisson of eigenvector approach (red,+) and polynomial approximation (yellow, ×) to solution with individual fibers (green,□).

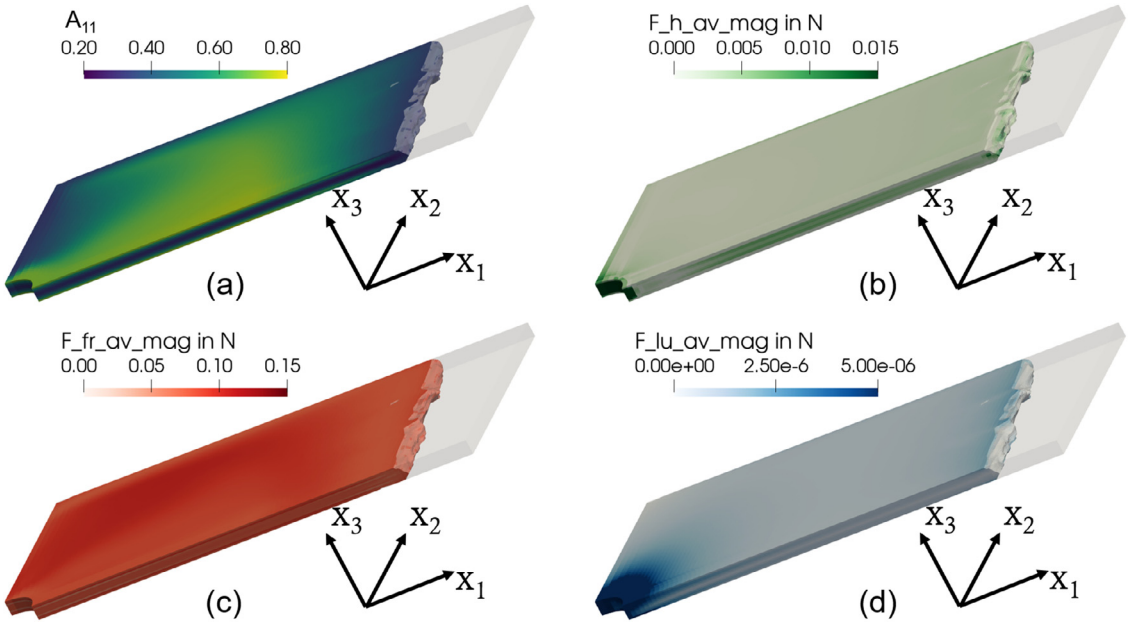

Fig. 12. Injection molding simulation results. Plate cut through the x_2-plane of symmetry (cf. Fig. 11) Fiber orientation component A_{11} (a), average hydrodynamic force magnitude (b), friction force magnitude (c) and lubrication force magnitude (d).

again the polynomial approach creates better results and is used in the simulations in Section 4.

4. 3D Injection molding simulation

4.1. 3D Injection molding simulation model

Injection molding simulations are performed on a square plate 3D-model. The geometry is given in Fig. 11. The plate is meshed with hexahedral elements having 1 mm in x_1- and x_2-direction and 0.3 mm in x_3-direction. The fibers' aspect ratio is chosen to 75, resulting in a fiber length of 1.125 mm, being similar to the simulation model used in [24]. The cavity is filled with a constant volume flow of 50 cm^3/s perpendicular to the inlet surface. According to [23] the value for k_{fr} is 0.3. The approach for the lubrication force is novel, so k_{lu} is also set to 0.3. This value is arbitrary, since it must be determined with experimental data, but within this work, only the principal distribution is regarded. The inlet boundary condition of the orientation tensor is $A_{11} = 0.8$ at the top and bottom walls (normal to the x_3-direction) and $A_{11} = 0.\bar{3}$ at the plane of symmetry in x_3-direction, with parabolic distribution in between. The other entries are $A_{22} = 4/5 \cdot (1 - A_{11})$, $A_{33} = 1/5 \cdot (1 - A_{11})$ and $A_{12} = A_{13} = A_{23} = 0$. All other material, orientation and flow models as well as boundary conditions and parameters are identical to the simulation model in our previous work [24].

4.2. 3D Injection molding simulation model results

Fig. 12 shows the results of the 3D injection molding simulation, specifically the fiber orientation as well as the average hydrodynamic, friction and lubrication forces. The forces show a reasonable distribution to the corresponding fiber orientation, being high orientated in flow direction near the walls and more randomly orientated in the core region. The hydrodynamic force is quite low near the walls and in the core center line, since $\Delta \boldsymbol{u}$ is low in these regions. The region with high hydrodynamic forces match with the zones where fiber breakage is observed in the process (near the walls and less in core regions), although the forces directly on the surface layers are lower. Here other effects like wall interactions are more important, but not content of this simulation. The friction force is higher within the core region, since it depends on $n^3_{c\phi}$ (Eq.(26) and Eq. (34)) and $n^3_{c\phi}$ is higher in less orientated regions, as shown in Section 3.3. Contrary to the other forces, the friction force is not higher near the inlet, since it is not depending on the absolute value of any relative velocity. The knowledge about fiber-fiber friction with respect to orientation may be the base for fiber-matrix separation, where this is an important aspect.

In contrast, the lubrication force shows higher values near the wall, in the high orientated regions, since the overlap area A_{ff} ascends with higher orientations grades and the velocity gradient is lower in the core region. Furthermore, the lubrication force is higher near the inlet, due to the higher velocity gradient. The higher velocity gradient also creates higher lubrication forces near the flow front, being not as high as in the wall near regions with higher degree of orientation, due to the lower A_{ff}.

Regarding the complete part all forces differ off about magnitudes, which is of course due to the change of velocity but also due to change of fiber orientation. Especially in case of friction force it is only due to change of fiber orientation, highlighting the importance of an orientation dependent modeling. Although these forces do not inflect the flow simulation within this work, they do in reality, leading to fiber breakage and fiber matrix separation. Of course, this also infects the stress distribution within the material and hence the complete flow and viscosity behavior of the material in the real process.

5. Conclusion

New approaches to approximate the forces acting on discontinuous fibers in polymer flow processes are presented. The forces comprise hydrodynamic drag and lift force (from fluid on fibers) as well as friction and lubrication forces (fiber contact forces). The latter two depend on the number of fiber-fiber contact points and on the contact area between the fibers. For friction force, the state-of-the-art approach is extended to consider both scalar invariants of orientation. The presented models are based on information provided by the second order fiber orientation tensor. The eigenvectors of the orientation tensor represent reference fibers, with the orientation probability of the corresponding eigenvalue. The reference fibers enable the calculation of averaged hydrodynamic forces with single fiber based existing approaches in macroscopic simulations. For calculation of contact forces, the contact points of the fibers

are needed. Therefore, two approaches, based on the reference fibers and a polynomial fit are presented to determine the average number of contact points within a fiber network. Here, the polynomial fit showed better results regarding different orientation states and fiber lengths. To approximate the lubrication force, an approach to determine the average fiber-fiber overlap within a fiber network is presented. The approach is based on the average fiber-fiber angle, which is determined based on the same models as the contact points.

To verify the new approaches, numerical experiments with individual fibers in different orientation states and lengths are performed. All approaches show good agreement with the numerical results. Furthermore, a 3D injection molding simulation is performed, showing reasonable distribution of the forces within the cavity in relation to the corresponding fiber orientation.

The new methods provide more information of the material state during processing, useful for ongoing works. The new knowledge of material internal forces can build the base for extension or modification of fiber orientation and fiber breakage models as well as fiber matrix separation models. Furthermore, the interaction forces can be considered in the momentum equation, which would enable a more detailed and realistic flow modelling. Additionally, future studies should focus on the macroscopic modeling of fiber bending forces, which are also an important process phenomenon with significant influence on the mentioned points. Besides the mentioned forces, further investigations in modeling of fiber-wall interactions are meaningful to further improve the prediction accuracy for molding simulation of fiber-reinforced polymer components.

Declaration of Competing Interest

The authors declare no conflict of interest.

Acknowledgements

This work has been carried out within the framework of the funded project Profilregion Mobilitätssysteme and ReMoS within the Innovationscampus Mobilität der Zukunft. The Profilregion Mobilitätssysteme is funded equally by the Ministry for Economy, Labor and Housing as well as the Ministry of Science, Research and Art of the state Baden-Württemberg, as well as through contributions from the Fraunhofer Society, the HsKa and the KIT. ReMoS is funded by the Ministry of Science, Research and Art of the state Baden-Württemberg.

We would like to thank the funders for the financial support.

Author Contributions

Florian Wittemann performed the conceptualization, investigation and methodology. He also wrote the first draft and revision of the paper. Luise Kärger supervised the methodology. Frank Henning supervised and performed the funding acquisition.

Appendix

The identity of the determination of f for the method presented in [17] (interactions tensor, IT) and the eigenvector (EV) based approach (Eq. (23)) will be shown here for the two orientation states 3D- quasi-isotropic and full alignment. Only these two states are regarded, since the exact formulation of the fourth order orientation tensor is known for these states.

It is

$$f_{\mathbf{EV}} = 2\lambda_1\lambda_2 + 2\lambda_1\lambda_3 + 2\lambda_2\lambda_3 \tag{A.1}$$

and

$$f_{\mathrm{IT}} = \delta_{ij}\left(A_{ij} - A_{ijkl}A_{kl}\right). \tag{A.2}$$

Full alignment:

In this case the eigenvalues are $\lambda_1 = 1$ and $\lambda_2 = \lambda_3 = 0$, so it is

$$f_{\mathrm{EV}} = 0. \tag{A.3}$$

According to [6] the fourth order orientation tensor for full alignment is given by $A_{ijkl} = A_{ij}A_{kl}$, so

$$f_{\mathrm{IT}} = \delta_{ij}\left(A_{ij} - A_{ij}A_{kl}A_{kl}\right), \tag{A.4}$$

with $A_{kl}A_{kl} = 1$ the final result is

$$f_{\mathrm{IT}} = \delta_{ij}\left(A_{ij} - A_{ij}\right) = 0. \tag{A.5}$$

3D- quasi-isotropic orientation

In this case the eigenvalues are $\lambda_1 = \lambda_2 = \lambda_3 = 1/3$, so it is

$$f_{\mathrm{EV}} = {}^{6}\!/_{9} = {}^{2}\!/_{3}. \tag{A.6}$$

According to [6] the fourth order orientation tensor for 3D- quasi-isotropic orientation is given by

$$\begin{aligned} A_{ijkl} = {}& {}^{-1}\!/_{35}\left(\delta_{ij}\delta_{kl} + \delta_{ik}\delta_{jl} + \delta_{il}\delta_{jk}\right) \\ & + {}^{1}\!/_{7}\left(A_{ij}\delta_{kl} + A_{ik}\delta_{jl} + A_{il}\delta_{jk} + A_{kl}\delta_{ij} + A_{jl}\delta_{ik} + A_{jk}\delta_{il}\right) \end{aligned} \tag{A.7}$$

Furthermore, it is

$$f_{\mathrm{IT}} = \delta_{ij}\left(A_{ij} - A_{ijkl}A_{kl}\right) = \delta_{ij}A_{ij} - \delta_{ij}A_{ijkl}A_{kl} = 1 - \delta_{ij}A_{ijkl}A_{kl} \tag{A.8}$$

and

$$\begin{aligned} \delta_{ij}A_{ijkl}A_{kl} = {}& {}^{-1}\!/_{35}\delta_{ij}\left(\delta_{ij}\delta_{kl} + \delta_{ik}\delta_{jl} + \delta_{il}\delta_{jk}\right)A_{kl} \\ & + {}^{1}\!/_{7}\delta_{ij}\left(A_{ij}\delta_{kl} + A_{ik}\delta_{jl} + A_{il}\delta_{jk} + A_{kl}\delta_{ij} + A_{jl}\delta_{ik} + A_{jk}\delta_{il}\right)A_{kl}. \end{aligned} \tag{A.9}$$

Simplifying the first term leads to

$$\begin{aligned} \text{first term} &= {}^{-1}\!/_{35}\left(\underbrace{\delta_{ij}\delta_{ij}}_{3}\underbrace{\delta_{kl}A_{kl}}_{1} + \underbrace{\delta_{ij}\delta_{ik}}_{\delta_{jk}}\underbrace{\delta_{jl}A_{kl}}_{A_{jk}} + \underbrace{\delta_{ij}\delta_{il}}_{\delta_{jl}}\underbrace{\delta_{jk}A_{kl}}_{A_{jl}}\right) \\ \text{first term} &= {}^{-1}\!/_{35}(3+1+1) = {}^{-1}\!/_{7}. \end{aligned} \tag{A.10}$$

Simplifying the second term leads to

$$\begin{aligned} &\text{second term} = \\ &= {}^{1}\!/_{7}\delta_{ij}\left(A_{ij}\delta_{kl} + A_{ik}\delta_{jl} + A_{il}\delta_{jk} + A_{kl}\delta_{ij} + A_{jl}\delta_{ik} + A_{jk}\delta_{il}\right)A_{kl} \\ &{}^{1}\!/_{7}\left(\underbrace{A_{ij}\delta_{ij}}_{1}\underbrace{\delta_{kl}A_{kl}}_{1} + \underbrace{\delta_{ij}A_{ik}}_{A_{jk}}\underbrace{\delta_{jl}A_{kl}}_{A_{jk}} + \underbrace{\delta_{ij}A_{il}}_{A_{jl}}\underbrace{\delta_{jk}A_{kl}}_{A_{jl}}\underbrace{\delta_{ij}A_{kl}\delta_{ij}A_{kl}}_{1} + \underbrace{\delta_{ij}A_{jl}}_{A_{il}}\underbrace{\delta_{ik}A_{kl}}_{A_{il}} + \underbrace{\delta_{ij}A_{jk}}_{A_{ik}}\underbrace{\delta_{il}A_{kl}}_{A_{ik}}\right) \\ &= {}^{1}\!/_{7}(1 + A_{jk}A_{jk} + A_{jl}A_{jl} + 1 + A_{il}A_{il} + A_{ik}A_{ik}) \\ &= {}^{1}\!/_{7}\left(1 + {}^{1}\!/_{3} + {}^{1}\!/_{3} + 1 + {}^{1}\!/_{3} + {}^{1}\!/_{3}\right) = {}^{10}\!/_{21}. \end{aligned} \tag{A.11}$$

Hence,

$$f_{\mathrm{IT}} = 1 + {}^{1}\!/_{7} - {}^{10}\!/_{21} = {}^{14}\!/_{21} = {}^{2}\!/_{3}. \tag{A.12}$$

References

[1] Keyser Hd, L-F Berg, J. Stammler, Composite materials ready to replace aluminium in internal combustion engines, JEC composites (53) (2016) 32–35.
[2] L Kärger, A Bernath, F Fritz, S Galkin, D Magagnato, A Oeckerath, et al., Development and validation of a CAE chain for unidirectional fibre reinforced composite components, Composite Struct. 132 (2015) 350–358.
[3] L Kärger, S Galkin, C Zimmerling, D Dörr, J Linden, A Oeckerath, et al., Forming optimisation embedded in a CAE chain to assess and enhance the structural performance of composite components, Compos. Struct. 192 (2018) 143–152.
[4] J Görthofer, N Meyer, TD Pallicity, L Schöttl, A Trauth, M Schemmann, et al., Virtual process chain of sheet molding compound: Development, validation and perspectives, Composites Part B: Eng. 169 (1) (2019) 133–147.
[5] SG Advani, CL. Tucker, The Use of Tensors to Describe and Predict Fiber Orientation in Short Fiber Composites, J. Rheol. 31 (8) (1987) 751–784.
[6] SG Advani, CL. Tucker, Closure approximations for three-dimensional structure tensors, J. Rheol. 34 (3) (1990) 367–386.
[7] Kwon. Chung, Fiber orientation in the processing of polymer composites, 2002.
[8] H Du Chung, TH Kwon, Invariant-based optimal fitting closure approximation for the numerical prediction of flow-induced fiber orientation, J. Rheol. 46 (1) (2002) 169–194.

[9] GB. Jeffery, The motion of ellipsoidal particles immersed in a viscous fluid, Proc. R. Soc. London 102 (1922) 161–179.
[10] F. Folgar, C.L. Tucker, Orientation behavior of fibers in concentrated suspensions, J. Reinf. Plast. Compos. 3 (1984) 98–119.
[11] J Wang, JF O'Gara, CL Tucker, An objective model for slow orientation kinetics in concentrated fiber suspensions: Theory and rheological evidence, J. Rheol. 52 (5) (2008) 1179–1200.
[12] JH Phelps, CL. Tucker, An anisotropic rotary diffusion model for fiber orientation in short- and long-fiber thermoplastics, J. Non Newtonian Fluid Mech. 156 (3) (2009) 165–176.
[13] N Meyer, L Schöttl, L Bretz, AN Hrymak, L. Kärger, Direct bundle simulation approach for the compression molding process of sheet molding compound, Composites, Part A 132 (2020) 105809.
[14] SB Lindström, T. Uesaka, Simulation of the motion of flexible fibers in viscous fluid flow, Phys. Fluids 19 (11) (2007) 113307.
[15] S. Englich, Strukturbildung bei der Verarbeitung von glasfasergefüllten Phenolformaldehydharzformmassen, Universitätsverlag Chennitz, Chemnitz, 2015.
[16] JP Hernandez, T. Raush, A Rios, S Strauss, TA Osswald, Theoretical analysis of fiber motion and loads during flow, Polym. Compos. 25 (1) (2004).
[17] J Férec, G Ausias, MC Heuzey, PJ. Carreau, Modeling fiber interactions in semiconcentrated fiber suspensions, J. Rheol. 53 (1) (2009) 49–72.
[18] N Meyer, O Saburow, M Hohberg, AN Hrymak, F Henning, L. Kärger, Parameter identification of fiber orientation models based on direct fiber simulation with smoothed particle hydrodynamics, J. Compos. Sci. 4 (2) (2020) 77.
[19] N Meyer, AN Hrymak, L. Kärger, Modeling Short-Range Interactions in Concentrated Newtonian Fiber Bundle Suspensions. Accepted for International Polymer Processing, but not published yet, 2021.
[20] S. Toll, Packing mechanics of fiber reinforcements, Polym. Eng. Sci. 38 (8) (1998) 1337–1350.
[21] Y Yamane, Y Kaneda, M. Dio, Numerical simulation of semi-dilute suspensions of rodlike particles in shear flow, J. Non Newtonian Fluid Mech. (54) (1994) 405–421.
[22] M Djalili-Moghaddam, S. Toll, A model for short-range interactions in fibre suspensions, J. Non Newtonian Fluid Mech. 132 (1-3) (2005) 73–83.
[23] C Servais, J-AE Månson, S. Toll, Fiber–fiber interaction in concentrated suspensions: Disperse fibers, J. Rheol. 43 (4) (1999) 991–1004.
[24] F Wittemann, R Maertens, L Kärger, F. Henning, Injection molding simulation of short fiber reinforced thermosets with anisotropic and non-Newtonian flow behavior, Composites, Part A 124 (2019) 105476.
[25] F Wittemann, R Maertens, A Bernath, M Hohberg, L Kärger, F. Henning, Simulation of reinforced reactive injection molding with the finite volume method, J. Compos. Sci. 2 (1) (2018) 5.
[26] X Fan, N Phan-Thien, R. Zheng, A direct simulation of fibre suspensions, J. Non Newtonian Fluid Mech. 74 (1-3) (1998) 113–135.
[27] SM Dinh, RC. Armstrong, A rheological equation of state for semiconcentrated fiber suspensions, J. Rheol. 28 (3) (1984) 207–227.
[28] S Toll, J-AE. Månson, Dynamics of a planar concentrated fiber suspension with non-hydrodynamic interaction, J. Rheol. 38 (4) (1994) 985–997.
[29] S Toll, J-AE. Månson, Elastic compression of a fibre network, J. Appl. Mech. 62 (1995) 223–226.